

# Spatial Analysis for AI-segmented Histopathology Images: Methods and Implementation

Yoolkyu Park<sup>1</sup>, Fangjiang Wu<sup>2</sup>, Xin Feng<sup>1</sup>, Shengjie Yang<sup>2</sup>  
Elizabeth H. Wang<sup>3</sup>, Bo Yao<sup>2</sup>, Chul Moon<sup>4</sup>, Guanghua Xiao<sup>2\*</sup>, and Qiwei Li<sup>1\*</sup>

<sup>1</sup>Department of Mathematical Sciences, The University of Texas at Dallas, Richardson, TX 75080

<sup>2</sup>School of Public Health, The University of Texas Southwestern Medical Center, Dallas, TX 75390

<sup>3</sup>Mays Business School, Texas A&M University, College Station, TX 77843

<sup>4</sup>Department of Statistics and Data Science, Southern Methodist University, Dallas, TX 75205

\*Corresponding authors

## Abstract

Quantitatively characterizing the spatial organization of cells and their interaction is essential for understanding cancer progression and immune response. Recent advances in machine intelligence have enabled large-scale segmentation and classification of cell nuclei from digitized histopathology slides, generating massive point pattern and marked point pattern datasets. However, accessible tools for quantitative analysis of such complex cellular spatial organization remain limited. In this paper, we first review 27 traditional spatial summary statistics, areal indices, and topological features applicable to point pattern data. Then, we introduce SASHIMI (Spatial Analysis for Segmented Histopathology Images using Machine Intelligence), a browser-based tool for real-time spatial analysis of artificial intelligence (AI)-segmented histopathology images. SASHIMI computes a comprehensive suite of mathematically grounded descriptors, including spatial statistics, proximity-based measures, grid-level similarity indices, spatial autocorrelation measures, and topological descriptors, to quantify cellular abundance and cell-cell interaction. Applied to two cancer datasets, oral potentially malignant disorders (OPMD) and non-small-cell lung cancer (NSCLC), SASHIMI identified multiple spatial features significantly associated with patient survival outcomes. SASHIMI provides an accessible and reproducible platform for single-cell-level spatial profiling of tumor morphological architecture, offering a robust framework for quantitative exploration of tissue organization across cancer types.

*Keywords:* Medical imaging, marked point pattern data, point pattern data, spatial statistics, topological data analysis

# 1 Introduction

Tissue morphology provides fundamental insights into organ function and disease mechanisms. In tumor tissues, the complex spatial arrangement of malignant and non-malignant cells forms the tumor microenvironment (TME) (Hanahan and Weinberg, 2011), which directly influences cancer progression, immune response, and therapeutic outcomes (Zhai et al., 2017; Wang et al., 2023). Histopathology imaging remains the gold standard for visualizing cellular and tissue-level morphological architecture, offering rich histological detail on nuclei, lymphocytes, glands, and stromal structures, together providing “a comprehensive view of disease and its effect on tissue” (Gurcan et al., 2009). Consequently, microscopic examination of hematoxylin and eosin (H&E)-stained slides is an essential step in the diagnosis and staging of numerous diseases. Yet this workflow relies heavily on expert pathologists to detect and interpret subtle spatial and morphological patterns within highly complex images. The process is time-consuming, subjective, and prone to substantial inter and intra-observer variability (Van Den Bent, 2010; Cooper et al., 2015).

The rapid advancement of artificial intelligence (AI) has reshaped histopathology imaging analysis, enabling quantitative, scalable, and reproducible assessment of complex tissue structures (Saltz et al., 2018; Corredor et al., 2019; Wang et al., 2019; Sobhani et al., 2022; Wang et al., 2022). Deep learning-based segmentation methods now delineate millions of individual cells from H&E-stained slides and automatically predict phenotypic or morphological labels that previously required manual pathologist annotation (Wang et al., 2019). As a result, characterizing cellular spatial organization and cell-cell interactions has become a central objective in modern computational pathology, though it remains challenging due to the inherent complexity and heterogeneity of tissue architecture. These AI-driven advances enable a shift from subjective, qualitative inspection to rigorous quantitative tissue modeling, allowing researchers to extract biologically and clinically meaningful imaging

biomarkers and features.

An AI-segmented histopathology image can be naturally represented as a marked point pattern, where each cell is characterized by its spatial coordinates and associated phenotypic or morphological label. This representation bridges digital pathology with spatial point pattern analysis and topological data analysis, providing a rigorous statistical framework for studying cellular spatial organization with the TME. A growing body of work shows that spatial correlation among cell types carry important prognostic value. For example, hierarchical Bayesian models have been used to quantify heterogeneous tumor-immune interactions, which are strongly associated with patient survival outcomes (Li et al., 2019a,b). More recent studies by Moon et al. (2023), Zhang et al. (2023), Stolz et al. (2024), and Zhang et al. (2024) demonstrate that geometric and topological descriptors capturing tissue shape can effectively stratify patient survival outcomes and characterize cellular and dynamical patterns. These findings underscore the clinical importance of quantifying multiscale cellular and architectural organization in tumor tissues through spatial and shape statistics.

Despite these methodological advances, there is still no systematic review of spatial and shape statistics for histopathology image analysis, and, more importantly, no online, integrative tool that enables researchers to efficiently quantify and visualize cellular spatial organization across large-scale AI-segmented histopathology images. Recent efforts, such as spatial pathology features (SPF) (Vu et al., 2022) and spatial quantification of pathology features (Spatial-QPFs) (Li, 2024), have demonstrated the clinical value of spatial summary statistics. However, these approaches rely on a limited set of spatial summary statistics and are available only as offline R packages, restricting usability and scalability.

To address these limitations, we first provide a comprehensive summary of 27 spatial summary statistics, areal indices, and topological features applicable to point pattern data. We

then introduce SASHIMI (Spatial Analysis of Segmented Histopathology Images using Machine Intelligence), a unified web-based platform that integrates these spatial and topological methods into a scalable, accessible, and reproducible analytical framework. SASHIMI focuses on integration, standardization, and real-time implementation of diverse analytical approaches for characterizing cellular spatial organization within tumor tissues. The platform encompasses three complementary analytical modules: (i) spatial summary statistics, capturing intercellular proximity and interaction patterns; (ii) topological and graph-based features, describing connectivity and structural complexity; and (iii) areal similarity indices, quantifying spatial heterogeneity across tissue compartments. Implemented as a real-time, browser-based interface, SASHIMI enables researchers to perform comprehensive exploratory spatial analyses without requiring extensive programming expertise. By applying SASHIMI to two case studies: (i) the oral potentially malignant disorder (OPMD) cohort from the Erlotinib Prevention of Oral Cancer (EPOC) trial at The University of Texas MD Anderson Cancer Center and (ii) the non-small-cell lung cancer (NSCLC) cohort from the National Lung Screening Trial (NLST), we demonstrate that spatial features derived through this integrated platform are significantly associated with patient survival outcomes. These findings highlight SASHIMI’s value as a practical and reproducible tool for quantitative digital pathology.

The remainder of this paper is organized as follows. Section 2 describes (marked) point pattern data extracted from histopathology images. Section 3 introduces the imaging feature extraction framework, covering spatial summary statistics, areal data indices, and topological features. Section 4 details the implementation of the SASHIMI online tool, including system design, input data requirements, output visualization modules, and user workflow. Section 5 presents two case studies, followed by a threshold-based significance analysis of the identified spatial biomarkers. Finally, Section 6 concludes the paper and

discusses potential directions for future research.

## 2 Data

### 2.1 Point Pattern Data

Let  $X = \{(x_1, y_1), \dots, (x_n, y_n)\}$  denote a spatial point pattern, where each coordinate  $(x_i, y_i) \in \mathbb{R}^2$  represents the coordinates of the  $i$ -th cell in a histopathology image, for  $i = 1, \dots, n$ .

### 2.2 Marked Point Pattern Data

A marked point pattern extends the point pattern framework by assigning a cell type to each point. Let  $X = \{(x_1, y_1, m_1), \dots, (x_n, y_n, m_n)\}$  denote a marked point pattern, where  $m_i \in M$  represents the cell type of the  $i$ -th point, and  $M = \{\text{tumor, stromal, lymphocyte}, \dots\}$  is the set of all observed cell types.

For each cell type  $m \in M$ , we define  $X_m = \{(x_i, y_i) | m_i = m\}$  as the subset of cells with type  $m$ . These subsets form a partition of the full point pattern:  $X = \bigcup_{m \in M} X_m$ . In the following, we use subscripts such as  $X_p, X_q$  and  $X_r$  to denote type-specific subsets, where  $p, q, r \in M$  indicate distinct cell types.

## 3 Imaging Features

We summarize 27 scalar and functional descriptors below, covering spatial summary statistics, areal indices, and topological features commonly used in point pattern analysis. A concise overview of each descriptor, including its definition and interpretability, is provided in Supplementary Table 1.

### 3.1 Spatial Summary Statistics

Spatial summary statistics are functions that analyze the spatial characteristics of points based on their locations and relationships. These functions characterize properties such as clustering, regularity, and inter-type spatial relationships (Baddeley et al., 2016). Given marked point pattern data extracted from segmented pathology images, SASHIMI automatically computes the corresponding spatial summary functions and produces graphical visualizations. Since computed spatial features are functional data, SASHIMI displays the computed functions alongside the input image, providing an intuitive visual interpretation of spatial organization.

The tumor tissue exhibits spatial heterogeneity across multiple scales, where cells may cluster locally while showing regular spacing at larger distances, and different cell types may exhibit attraction, repulsion, or independence. To capture this complexity, SASHIMI computes a comprehensive suite of spatial summary statistics organized into function families, providing both univariate analyses of single cell types and bivariate analyses of inter-type interactions. For example, Ripley’s  $K$ -function (Ripley, 1977) quantifies the expected number of neighboring points within distance  $r$  of a typical point, revealing clustering or dispersion patterns. The  $G$ -function characterizes the distribution of nearest-neighbor distances, while the  $J$ -function combines inter-point and empty-space information to detect deviations from complete spatial randomness.

All spatial summary statistics in SASHIMI are computed using the R package `spatstat` (Baddeley et al., 2016), which implements rigorous edge-correction methods to mitigate boundary effects in finite observation windows.

### 3.1.1 $K$ and $L$ -functions

The  $K$ -function is a second-order spatial summary statistic that quantifies the expected number of additional points within a distance  $r$  of a typical point, normalized by the overall intensity  $\lambda$  of the process. Formally, for a stationary point process, it is defined as:

$$K(r) = \frac{1}{\lambda} \mathbb{E}[\text{number of further points within distance } r \text{ of a typical point}]$$

Under a homogeneous Poisson process (i.e., complete spatial randomness), this simplifies to  $K(r) = \pi r^2$ . Deviations from this theoretical curve reveal departures from spatial randomness: when  $K(r) > \pi r^2$ , the pattern exhibits spatial clustering, whereas  $K(r) < \pi r^2$  indicates spatial inhibition or regularity.

#### Ripley's $K$ -function

Ripley's  $K$ -function is given by:

$$K(r) = \frac{1}{\lambda} \sum_j \sum_{i \neq j} I_r(d_{ij}) w_i, \quad \lambda = \frac{N}{A} \quad (1)$$

where  $N$  is the total number of points and  $A$  is the area of the region, which is 1 when normalized. The Euclidean distance between two points  $(x_i, y_i)$  and  $(x_j, y_j)$  is  $d_{ij} = \sqrt{(x_i - x_j)^2 + (y_i - y_j)^2}$ . The indicator function  $I_r(d_{ij})$  equals 1 if  $d_{ij} \leq r$  and 0 otherwise. Ripley's isotropic correction weight  $w_{ij} = 1/e_{ij}$  provides an isotropic edge correction, where  $e_{ij}$  denotes the proportion of the circumference of the circle centered at  $(x_i, y_i)$  with radius equal to the inter-point distance  $d_{ij}$  that lies within the observation window.

#### Directional $K$ -function

The directional  $K$ -function considers spatial patterns along specific directions:

$$K_\theta(r) = \frac{1}{\lambda} \sum_j \sum_{i \neq j} I_r(d_{ij}) \cdot I_\theta(\angle_{ij}) w_{ij} \quad (2)$$

where  $I_\theta(\angle_{ij})$  ensures that only pairs within the directional range  $\theta - \frac{\Delta\theta}{2} \leq \angle_{ij} < \theta + \frac{\Delta\theta}{2}$



are considered.

### Cross-type $K$ -function

The cross-type  $K$ -function evaluates spatial relationships between different categories of points:

$$K_{\text{cross}}(r) = \frac{1}{\lambda_q} \sum_{i \in X_p} \sum_{j \in X_q} I_r(d_{ij}) w_{ij} \quad (3)$$

where  $\lambda_q$  denotes the intensity of the point process of type  $q$ .

### Mark Weighted $K$ -function

The mark weighted  $K$ -function extends Ripley's  $K$ -function by incorporating weights based on spatial point attributes, its mark value:

$$K_f(r) = \frac{1}{\lambda f(M, M')} \sum_i \sum_{j \neq i} f(m_i, m_j) I_r(d_{ij}), \quad (4)$$

where  $f(m_i, m_j)$  is a user-defined weight function (by default  $f(m_i, m_j) = m_i m_j$ ).

### Scaled $K$ -function ( $L$ -function)

The scaled  $K$ -function, also known as the  $L$ -function, normalizes  $K(r)$  to remove dimensional effects:

$$L(r) = \sqrt{\frac{K(r)}{\pi}} \quad (5)$$

so that  $L(r) > r$  indicates spatial clustering and  $L(r) < r$  indicates spatial inhibition or regularity. This function normalizes the traditional  $K$ -function, removing dimensionality effects.

### Cross-type $L$ -function

The cross-type  $L$ -function captures spatial correlations between points with different marks, extending the concept of the scaled  $K$ -function:

$$L_{\text{cross}}(r) = \sqrt{\frac{K_{\text{cross}}(r)}{\pi}} \quad (6)$$

### 3.1.2 $G$ , $F$ , and $J$ -Functions

The  $G$ -function, or nearest-neighbor distribution function, describes the cumulative distribution of distances from each point in the pattern to its nearest neighboring point. It takes values in  $[0, 1]$ . Under complete spatial randomness (CSR) with intensity  $\lambda$ , the theoretical form is

$$G_{\text{CSR}}(r) = 1 - \exp(-\lambda\pi r^2). \quad (7)$$

Departures from this theoretical curve reveal deviations from spatial randomness: when  $G(r)$  lies above  $G_{\text{CSR}}(r)$ , the pattern exhibits clustering (an excess of short inter-point distances), whereas values below  $G_{\text{CSR}}(r)$  indicate inhibition (a deficiency of close neighbors). Additionally,  $F$ -function follows the same nature.

#### **$G$ -function**

The  $G$ -function captures empty spaces between points by measuring the nearest neighbor distance from each point. The empirical estimator of  $G(r)$  is

$$G(r) = \frac{1}{N} \sum_{i=1}^N I_r(d_i), \quad (8)$$

where  $d_i = \min_{j \neq i} d_{ij}$  is the distance from point  $i$  to its nearest neighbor,  $d_{ij} = \sqrt{(x_i - x_j)^2 + (y_i - y_j)^2}$  is the Euclidean distance between points  $i$  and  $j$ , and  $I_r(d_i) = 1$  if  $d_i \leq r$  and 0 otherwise.

#### **Cross-type $G$ -Function**

The cross-type  $G$ -function quantifies the distribution of nearest-neighbor distances from points of type  $p$  to points of type  $q$ :

$$G_{\text{cross}}(r) = \frac{1}{N_p} \sum_{i \in X_p} I_r(d_{i,q}), \quad (9)$$

where for each point  $i \in X_p$ , the distance  $d_{i,q}$  is defined as  $d_{i,q} = \min_{j \in X_q} d_{ij}$ . Here,  $I_r(d_{i,q}) = 1$  if  $d_{i,q} \leq r$  and 0 otherwise.

### ***F*-function**

The *F*-function, similarly, measures the empty space in the point process pattern, but uses the distance from a randomly chosen point  $u$  to its nearest neighbor:

$$F(r) = \frac{1}{N} \sum_u I_r(d(u)) \quad (10)$$

where the empty-space distance from a randomly chosen reference point  $u$  to its nearest neighbor  $i$  is  $d(u) = \min\{\|(x_u, y_u) - (x_i, y_i)\|\}$ .

### **Cross-type *F*-function**

The Cross-type *F*-function measures the distance from a randomly reference chosen point  $u$  to its nearest type  $q$  neighbor  $j$ :

$$F_{\text{cross}}(r) = \frac{1}{N} \sum_u I_r(d(u, j)) \quad (11)$$

where the empty-space distance from a randomly chosen reference point  $u$  to its nearest type  $q$  neighbor  $j$  is  $d(u, j) = \min\{\|(x_u, y_u) - (x_j, y_j)\|\}$ .

### ***J*-function**

The *J*-function is a dimensionless ratio of two functions,  $G(r)$  and  $F(r)$ , and is given by:

$$J(r) = \frac{1 - G(r)}{1 - F(r)} \quad (12)$$

Under CSR,  $J(r) \equiv 1$  for all  $r$ . Values of  $J(r)$  below 1 indicate clustering (an excess of short distances), whereas values above 1 indicate regularity or inhibition. Because it integrates both the inter-point ( $G$ ) and empty-space ( $F$ ) perspectives, the *J*-function is less sensitive to variations in point density and provides a scale-independent measure of spatial structure.

### **Cross-type *J*-function**

Similarly, the cross-type  $J$ -function is given by:

$$J_{\text{cross}}(r) = \frac{1 - G_{\text{cross}}(r)}{1 - F_{\text{cross}}(r)} \quad (13)$$

### 3.1.3 Correlation Functions

#### Pair Correlation Function (PCF)

The pair correlation function (PCF) provides a noncumulative measure of spatial dependence, complementary to Ripley's  $K$ -function. While  $K(r)$  summarizes the cumulative number of neighboring points within distance  $r$ , the PCF, denoted  $\text{pcf}(r)$ , captures the local intensity of points exactly at distance  $r$  from a typical point. Formally, it is defined as

$$\text{pcf}(r) = \frac{1}{2\pi r} \frac{dK(r)}{dr}, \quad (14)$$

where  $K(r)$  is the Ripley's  $K$ -function introduced previously. For a homogeneous Poisson process under complete spatial randomness (CSR),  $\text{pcf}(r) \equiv 1$ . Values  $\text{pcf}(r) > 1$  indicate spatial clustering (an excess of pairs at distance  $r$ ), whereas  $\text{pcf}(r) < 1$  indicate inhibition or regularity (a deficit of pairs at that scale).

#### Cross-type Pair Correlation Function

The cross-type PCF, denoted by  $\text{pcf}_{\text{cross}}(r)$ , quantifies the spatial dependence between two distinct point types. It is obtained analogously from the cross-type  $K$ -function:

$$\text{pcf}_{\text{cross}}(r) = \frac{1}{2\pi r} \frac{dK_{\text{cross}}(r)}{dr}. \quad (15)$$

Here,  $K_{\text{cross}}(r)$  measures the cumulative spatial interaction between two cell types, and its derivative  $\text{pcf}_{\text{cross}}(r)$  reflects the strength of inter-type correlation at distance  $r$ . Under CSR,  $\text{pcf}_{\text{cross}}(r) = 1$  for all  $r$ ; values above one suggest attraction between the two types, whereas values below one imply spatial segregation.

#### Mark Connected Function

When each point carries a quantitative or categorical mark  $m_i$ , the mark correlation function extends the PCF to assess correlations among marks at given distances. Let  $f(m_i, m_j)$  denote a user-defined weighting function (e.g., product, indicator, or correlation of marks). The MCF is then expressed as

$$\text{mcf}_r = \frac{\lambda_p \lambda_q \text{pcf}_{\text{cross}}(r)}{\lambda^2 \text{pcf}(r)} \quad (16)$$

where  $\lambda_p$  and  $\lambda_q$  are the intensities of the corresponding point types,  $\lambda$  is the overall process intensity. Values  $\text{mcf}_r > 1$  indicate positive mark association (similar marks occur more frequently nearby), whereas  $\text{mcf}_r < 1$  suggest negative association or mark repulsion.

## 3.2 Areal Data Indices

SASHIMI also computes spatial autocorrelation and similarity indices based on grid-level representations of the tissue. The marked point pattern data are tessellated into a  $Q \times Q$  quadrat count matrix (e.g.,  $Q = 20$ ), transforming the continuous spatial distribution into a discrete areal format. This representation enables quantification of spatial structure through statistics that assess cell-type aggregation, dispersion, and compositional similarity across tissue regions.

We denote by  $Q_X$  a  $20 \times 20$  quadrat count grid computed from the original point pattern  $X$ . Type-specific quadrat counts are written as  $Q_{Xp}, Q_{Xq}, Q_{Xr}$ , etc. Let  $Q_X[i]$  denote the count in the  $i$ th quadrat of  $Q_X$ , and let  $n$  be the number of quadrats ( $n = 400$  for a  $20 \times 20$  grid).

### 3.2.1 Spatial autocorrelation measures

Spatial autocorrelation measures quantify the degree of spatial dependence between neighboring quadrats. These include Moran's I ([Moran, 1950](#)), Geary's C ([Geary, 1954](#)), and the Quadrat Count Statistic, which assess whether quadrats with similar cell densities tend

to cluster spatially or exhibit random or dispersed patterns.

### **Moran's I**

Moran's I is another widely used measure of global spatial autocorrelation and is inversely related to Geary's C. It is defined as

$$\text{MoranI} = \frac{N}{S_0} \frac{\sum_i \sum_j w_{ij} (x_i - \bar{x})(x_j - \bar{x})}{\sum_i (x_i - \bar{x})^2} \quad (17)$$

where the notations  $x_i$ ,  $\bar{x}$ , and  $w_{ij}$  follow those in the definition of Geary's C. Positive values of Moran's I indicate clustering of similar cell densities, values near 0 indicate randomness, and negative values suggest spatial dispersion.

### **Geary's C**

Geary's C is a global measure of spatial autocorrelation that evaluates the similarity between neighboring quadrats.

Let  $N$  denote the total number of quadrats,  $x_i$  the cell count in the  $i$ th quadrat of  $Q_X$ , and  $\bar{x}$  the mean of  $x_i$ . Then Geary's C is defined as

$$\text{GearyC} = \frac{(N-1) \sum_i \sum_j w_{ij} (x_i - x_j)^2}{2S_0 \sum_i (x_i - \bar{x})^2} \quad (18)$$

where the spatial weights matrix is defined as  $w_{ij} = 1$  if quadrat  $i$  is a neighbor of  $j$ , and  $w_{ij} = 0$  otherwise. The total sum of weights is  $S_0 = \sum_{i=1}^N \sum_{j=1}^N w_{ij}$ . Values of Geary's C range from 0 to values greater than 1. A value close to 0 indicates strong positive spatial autocorrelation (neighboring quadrats are similar), while values greater than 1 indicate negative spatial autocorrelation (neighboring quadrats are dissimilar).

### **Lee's L**

Lee's  $L$  is a spatial correlation coefficient that measures the association between two sets of observations in the same spatial domain. Unlike the standard Pearson correlation, Lee's  $L$  incorporates spatial dependence *via* a spatial weights matrix. Let  $x_i$  and  $y_i$  denote the

counts of two different cell types in the  $i$ th quadrat, and  $\bar{x}$ ,  $\bar{y}$  their respective means. Lee's  $L$  is given by

$$\text{Lee's } L = \frac{N}{\sum_i (\sum_j w_{ij})^2} \frac{\sum_i \sum_j (\tilde{x}_i - \bar{x})(\tilde{y}_i - \bar{y})}{\sqrt{\sum_i (\tilde{x}_i - \bar{x})^2} \sqrt{\sum_i (\tilde{y}_i - \bar{y})^2}} \quad (19)$$

where  $\tilde{x}_i = \sum_j w_{ij} x_j$ ,  $\tilde{y}_i = \sum_j w_{ij} y_j$ , and  $w_{ij}$  denotes spatial adjacency between quadrats  $i$  and  $j$ . A higher Lee's  $L$  value indicates stronger positive spatial correlation between the two variables.

### Quadrat Count Statistic

The quadrat test assesses deviations from complete spatial randomness (CSR) by comparing observed and expected cell counts across quadrats:

$$X^2 = \sum_{i=1}^n \frac{(O_i - E_i)^2}{E_i} \quad (20)$$

where  $O_i$  and  $E_i$  are the observed and expected counts in the  $i$ th quadrat under CSR. The test statistic  $X^2$  is compared to a chi-squared reference distribution to evaluate the null hypothesis  $H_0$ : quadrat counts follow a Poisson distribution implied by CSR.

### Join Count Statistic

The join count statistic evaluates spatial association (autocorrelation) for binary categorical maps. For a chosen pair of cell types  $p$  and  $q$ , define a binary indicator  $b_i \in \{0, 1\}$  on each quadrat (e.g.,  $b_i = 1$  if type  $p$  is present in the  $i$ th quadrat and  $b_i = 0$  otherwise), and let  $w_{ij}$  be the spatial adjacency indicator between quadrats  $i$  and  $j$ :

$$w_{ij} = \begin{cases} 1, & \text{if } i \text{ is a neighbor of } j, \\ 0, & \text{otherwise.} \end{cases} \quad (21)$$

The counts of like-like and unlike joins are

$$J_{pp} = \frac{1}{2} \sum_{i \neq j} w_{ij} b_i b_j, \quad J_{pq} = \frac{1}{2} \sum_{i \neq j} w_{ij} (b_i - b_j)^2, \quad J_{qq} = \frac{1}{2} \sum_{i \neq j} w_{ij} (1 - b_i)(1 - b_j), \quad (22)$$

and the total number of joins is  $J = J_{pp} + J_{pq} + J_{qq}$ . Here the factor  $1/2$  avoids double counting under an undirected neighbor graph. The choice of contiguity (e.g., rook vs. queen) determines  $w_{ij}$ .

### 3.2.2 Similarity indices

Similarity indices measure compositional overlap or dissimilarity between spatial distributions of different cell types. SASHIMI computes the Jaccard Index, the Morisita-Horn Index ([Morisita, 1962](#)), and cosine similarity to quantify the degree of co-localization among cell types within tissue regions.

#### Tanimoto Coefficient

The Tanimoto coefficient (generalized Jaccard for vectors) index measures the similarity between type-specific quadrat count vectors and is computed only on quadrats where at least one of the two types is present. For types  $p$  and  $q$ , let  $Q_{Xp}$  and  $Q_{Xq}$  be the corresponding quadrat count vectors (restricted to the selected quadrats). The coefficient is

$$T(Q_{Xp}, Q_{Xq}) = \frac{Q_{Xp}^\top Q_{Xq}}{\|Q_{Xp}\|_2^2 + \|Q_{Xq}\|_2^2 - Q_{Xp}^\top Q_{Xq}} \quad (23)$$

with range  $0 \leq T(Q_{Xp}, Q_{Xq}) \leq 1$ , where  $T = 1$  indicates identical distributions and  $T = 0$  indicates no overlap.

#### Dice - Sorensen Index (Vector Form)

The Sorensen index quantifies similarity between two quadrat count distributions and can be expressed in vector form as:

$$\text{DSC}(Q_{Xp}, Q_{Xq}) = \frac{2Q_{Xp}^\top Q_{Xq}}{\|Q_{Xp}\|_2^2 + \|Q_{Xq}\|_2^2} \quad (24)$$

When the counts are binary, this expression reduces to the classical Dice–Sorensen index. The coefficient ranges between 0 and 1, where 1 indicates identical distributions and 0 indicates no overlap.



## Morisita-Horn Index

The Morisita-Horn index measures compositional overlap between two quadrat count distributions, accounting for differences in abundance:

$$MH = \frac{2 \sum_{i=1}^N Q_{Xp}[i] Q_{Xq}[i]}{\sum_{i=1}^N (Q_{Xp}[i])^2 + \sum_{i=1}^N (Q_{Xq}[i])^2} \quad (25)$$

Prior to computation, both quadrat count vectors are normalized by their total counts:

where both quadrats  $Q_{Xp}, Q_{Xq}$  are normalized as:

$$Q_{Xp} = \frac{Q_{Xp}}{|Q_{Xp}|}, \quad Q_{Xq} = \frac{Q_{Xq}}{|Q_{Xq}|}. \quad (26)$$

The index takes values in  $[0, 1]$ , where higher values indicate greater similarity between spatial compositions.

## Clark and Evans Aggregation Index

The Clark and Evans Aggregation Index quantifies the degree of clustering or regularity in a spatial point process:

$$R = \frac{\bar{r}_o}{\bar{r}_e} \quad (27)$$

where  $\bar{r}_o$  is the average of the observed nearest distance from point  $i$  and  $\bar{r}_e$  is its theoretical expectation under complete spatial randomness (CSR). The observed mean distance is computed as  $\bar{r}_o = \frac{1}{N} \sum d_i$ , where  $N$  is the total number of points and  $d_i$  is the nearest-neighbor distance from point  $i$ . Under CSR, the expected mean nearest-neighbor distance is  $\bar{r}_e = \frac{1}{2\sqrt{\lambda}}$  where  $\lambda$  is the intensity of the point pattern. An  $R$  value close to 1 indicates a random (CSR) distribution;  $R < 1$  suggests clustering or aggregation; and  $R > 1$  indicates spatial regularity or inhibition.

## Bhattacharyya Coefficient

The Bhattacharyya coefficient quantifies the degree of overlap between two discrete probability distributions. For two normalized quadrat count distributions  $Q_{Xp}$  and  $Q_{Xq}$ , it is

defined as

$$\text{BC} = \sum_i \sqrt{Q_{Xp}[i]Q_{Xq}[i]} \quad (28)$$

Computes the probability of two distributions from the same discrete domain  $Q_X$ , overlap. where:

$$Q_{Xp}[i] = \frac{\text{number of points in the } i\text{-th grid in } Q_{Xp}}{\text{number of all points in } Q_{Xp}}$$

$$Q_{Xq}[i] = \frac{\text{number of points in the } i\text{-th grid in } Q_{Xq}}{\text{number of all points in } Q_{Xq}}$$

The coefficient ranges from 0 to 1, where  $\text{BC} = 1$  indicates identical distributions and  $\text{BC} = 0$  indicates no overlap.

### Cosine Similarity

Cosine similarity measures the angular similarity between two nonzero vectors. For two feature vectors  $Q_{Xp}$  and  $Q_{Xq}$ , it is defined as

$$\text{Cossim}(Q_{Xp}, Q_{Xq}) = \frac{\sum_i Q_{Xp}[i]Q_{Xq}[i]}{\sqrt{\sum_i (Q_{Xp}[i])^2} \sqrt{\sum_i (Q_{Xq}[i])^2}}. \quad (29)$$

Its values range from  $-1$  to  $1$ , where  $1$  indicates perfect alignment (maximum similarity),  $0$  indicates orthogonality (no relationship), and  $-1$  indicates perfect opposition.

Together, these measures provide complementary perspectives on spatial organization: autocorrelation statistics capture global patterns of spatial dependence, while similarity indices describe local compositional relationships. All computed metrics are returned as scalar features in a single-row data frame. Computations are supported by the R packages `spatstat` ([Baddeley et al., 2016](#)) and `spdep` ([Bivand et al., 2015](#)).

### 3.3 Topological Features

Topology, a branch of mathematics that focuses on spaces that are invariant under continuous transformations, forms the basis of topological data analysis (TDA). It enables characterization of spatial patterns through topological features such as the number of

connected components (dimension zero features) and loops (dimension one features). In SASHIMI, topological features of marked point pattern data are computed using persistent homology with the witness complex, a method that approximates the shape of the data by encoding its local connectivity structure (De Silva and Carlsson, 2004). The resulting output is represented as a multiset of birth–death intervals. From these intervals, we extract summary statistics that quantitatively characterize the topological features across multiple spatial scales. For each dimension, we compute distributional statistics of birth times, death times, and feature lifetimes, including their minima, maxima, means, and standard deviations, along with the total number of detected features. This functional representation provides a complementary view of the spatial organization beyond classical distance-based descriptors. Computations are performed using the Python package GUDHI (The GUDHI Project, 2025).

### Witness Complex

Let  $L \subset X$  denote a set of *landmark points* and  $W \subset X$  a set of *witness points*, where  $X$  is the full point pattern. The witness complex  $W(L, W, \varepsilon)$  approximates the geometric shape of the data by encoding its local connectivity structure. Formally, a  $k$ -dimensional simplex  $\sigma = \{l_0, \dots, l_k\} \subseteq L$  is included in the witness complex if there exists a witness  $w \in W$  such that all vertices of  $\sigma$  lie within a distance  $\varepsilon$  of  $w$ :

$$\exists w \in W \quad \text{s.t.} \quad \max_{l_i \in \sigma} d(w, l_i) \leq \varepsilon.$$

This construction efficiently captures the topological relationships between the landmark and witness subsets while reducing computational complexity relative to full Vietoris–Rips complexes.

In our application, cells of type A are selected as landmarks and cells of type B as witnesses. This asymmetric construction emphasizes how one cell population is geometrically arranged relative to the other. We use three types of cells for the witness complex: tumor,

immune, and stromal. Therefore, the resulting persistent homology reflects cross-scale structural interplay, such as between tumor and immune or stromal components.

## 4 Online Tool Implementation

### 4.1 Implementation

SASHIMI is a browser-based computational framework implemented in **R** and **Python** for the extraction, visualization, and computation of spatial features from AI-segmented histopathology images, enabling real-time analysis. The platform functions as both an exploratory and feature-extraction tool, generating two complementary forms of output from marked point pattern data: (i) functional visualizations, which characterize distance-dependent spatial dynamics (e.g., Ripley’s  $K$ -function and pair correlation function), and (ii) scalar indices, which quantify spatial autocorrelation and compositional similarity across tissue regions (e.g., Moran’s  $I$ , Jaccard index, and summary statistics derived from persistence diagrams). Together, these outputs provide a comprehensive and interpretable representation of the spatial organization and topological structure of tumor tissue architecture.

### 4.2 Input Requirements and Data Format

SASHIMI accepts tabular data in CSV format with a maximum file size of 4 MB. Each input file must contain three columns corresponding to the  $x$ -coordinate,  $y$ -coordinate, and cell type. Upon upload, the data are displayed as a point cloud, where each point represents an individual cell on the tissue slide and is color-coded by cell type. Users may select up to three cell types for analysis. For each selection, SASHIMI computes both single-type spatial features and pairwise cross-type spatial functions.

### 4.3 Output Types and Visualization

SASHIMI produces two forms of output. Functional outputs consist of spatial summary statistics rendered as plots, enabling interpretation of distance-based spatial relationships. Scalar outputs include autocorrelation measures, similarity indices, and summary statistics of the persistence diagram. Returned in tabular form, it provides quantitative measures suitable for direct comparison and statistical analysis. All computed features can be downloaded in CSV format for downstream use.

### 4.4 User Workflow

The overall analytical workflow of the SASHIMI is illustrated in Figure 1, which outlines the end-to-end computational process from raw histopathology images to quantitative spatial features. SASHIMI operates through three intuitive steps: (1) uploading marked point pattern data; (2) selecting desired spatial feature categories; and (3) visualizing and downloading the computed results.

The corresponding web interface of SASHIMI is shown in Figure 2, which demonstrates the user-facing implementation of this pipeline. Panel (A) shows the home and overview interface, where users are introduced to the purpose and functionality of SASHIMI through concise descriptions and navigation links. Panel (B) displays the online analysis interface, where users can upload one or two point-pattern files (e.g., different cell types or tissue regions), specify functional statistics such as the  $K$ -function, and submit the job for computation. Panel (C) illustrates the output interface, which presents both areal-level spatial maps and functional summary plots (e.g.,  $K$ -,  $G$ -, and  $L$ -functions), along with downloadable CSV tables containing all computed indices.

Together, these components provide a seamless and reproducible environment for quantitative spatial analysis of AI-segmented histopathology images. SASHIMI is freely accessible

as a web application at <https://lce.biohpc.swmed.edu/sashimi/>, with full source code and documentation available at <https://github.com/hangookminsokchon/SASHIMI>.

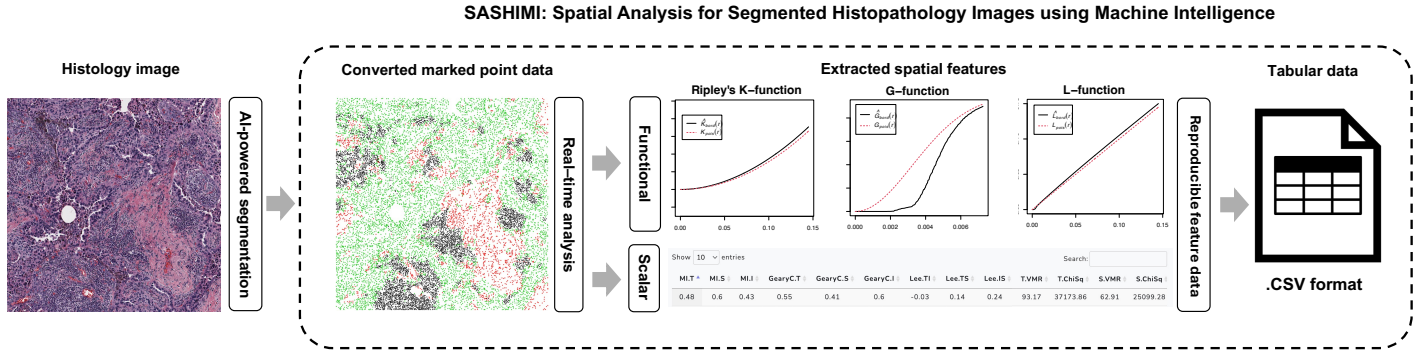


Figure 1: SASHIMI workflow

## 5 Case Studies

To examine the relationship between cellular spatial organization and patient survival outcomes, we analyzed two real-world datasets: lung cancer pathology images from NSCLC patients in the NLST and oral tissue pathology images from OPMD patients in the EPOC trial at The University of Texas MD Anderson Cancer Center.

To evaluate the prognostic relevance of spatial features, functional Cox proportional hazards (FCoxPH) models were fitted using the **survival** package in R. Patient ID was used as a clustering variable to account for within-patient correlations arising from multiple image regions. Each spatial feature was modeled individually, with patient age and cancer stage included as additional scalar covariates. Statistical significance was assessed across multiple thresholds to identify spatial descriptors potentially associated with patient prognosis.

To characterize distance-dependent spatial dynamics, we applied functional principal component analysis (FPCA) to the computed functional descriptors. Spatial functions were

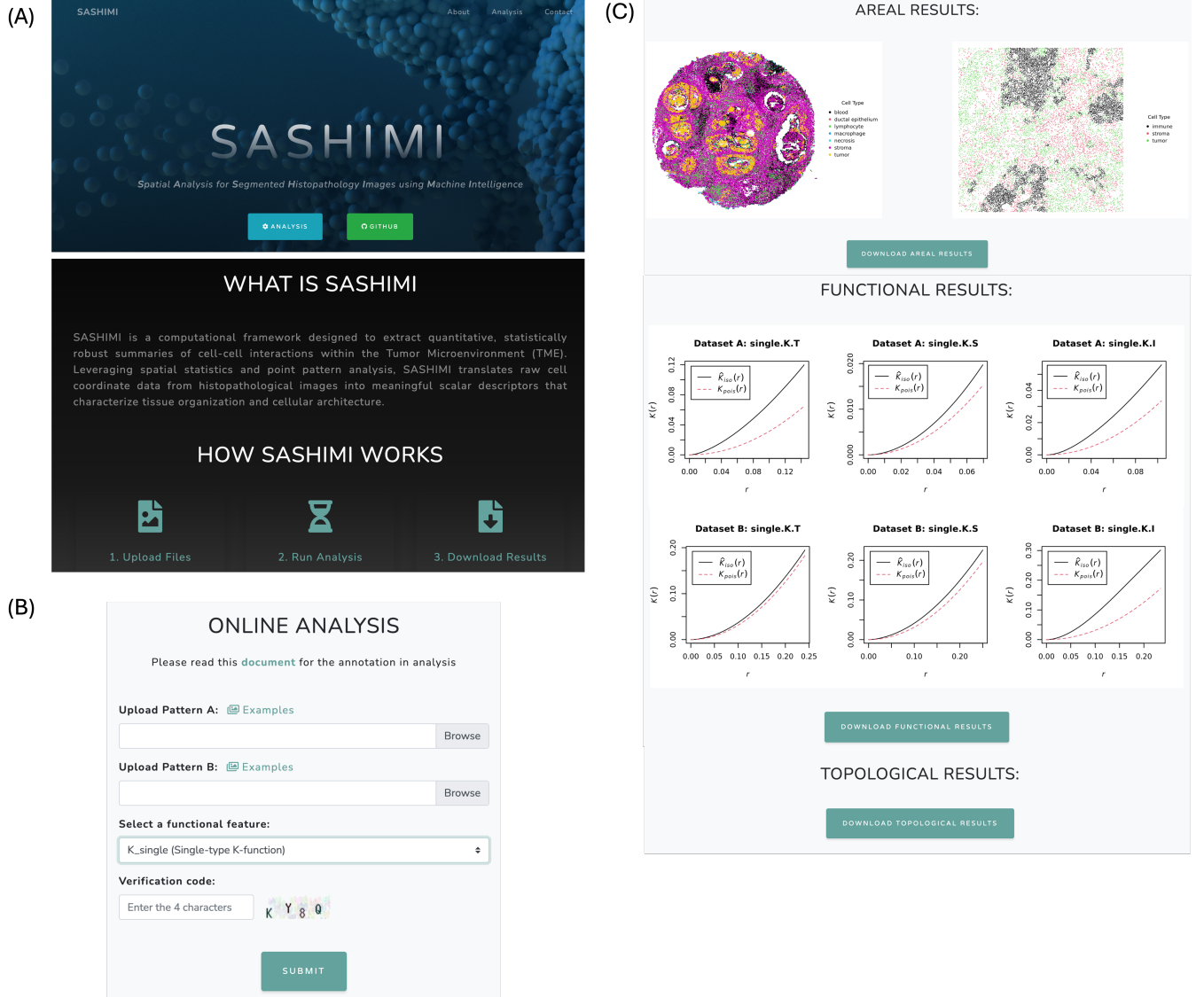


Figure 2: User interface of the SASHIMI web application. (A) Home and overview interface introducing the framework and navigation structure; (B) Online analysis page for uploading point-pattern data and selecting spatial features; (C) Output page displaying areal-level maps and functional results with download options.

decomposed using FPCA based on the Karhunen–Loève expansion (Kong et al., 2018), and the first two principal components, which captured approximately 90% of the total variance, were retained. The resulting FPCA scores were then used as covariates in the survival analysis models, along with additional scalar covariates. Additional methodological details are provided in the supplementary materials.

## 5.1 Case Study I: Lung Cancer Pathology Images

The NLST dataset comprised 345 tumor images from 188 patients, acquired from the National Lung Screening Trial (NLST) conducted by the National Cancer Institute. All images were formalin-fixed paraffin-embedded (FFPE) slides captured at  $40\times$  magnification. Following segmentation, 1585 image regions were obtained, each containing approximately 12,000 individual cell points. For model fitting, 1578 images were used after excluding seven images with missing cell-type annotations.

Several spatial features demonstrated statistically significant associations with survival outcomes. Table 1 summarizes the main predictors identified at different  $p$ -value thresholds, spanning classical spatial statistics, topological descriptors, and areal indices. The complete set of results is provided in Supplementary Table 2.

At the most stringent level ( $p < 0.05$ ), two topological features and one spatial summary statistic feature were identified. Specifically, `witness_tumor_stromal_h0_lifetime_max` and `witness_tumor_stromal_h0_death_std` emerged as highly significant, underscoring the relevance of connected-component persistence in tumor-stromal organization. In addition, the `PCF.CROSS.T2I.PC1` captured pairwise correlation dynamics between tumor and immune cells.

When the threshold was relaxed to  $p < 0.10$ , additional predictors became significant, including `MK.CONN.S2I.PC2` and `L.CROSS.T2I.PC1`, both reflecting cross-type clustering dy-



namics, as well as two topological  $H_1$  features, `witness_immune_stromal_h1_birth_std` and `witness_tumor_immune_h1_death_mean` representing the variability and persistence of loops across immune-stromal and tumor-immune interactions.

At  $p < 0.15$ , further single-type and scalar indices (J.REP.I.PC1, G.CROSS.T2I.PC1, MH.IS) were identified, along with an additional cross-type  $K$ -function (K.CROSS.T2S.PC2). By  $p < 0.20$ , a broader set of spatial and topological descriptors reached significance, including additional cross-type  $K$ -,  $J$ -,  $F$ -, and  $G$ -functions.

Collectively, these findings demonstrate that both conventional spatial statistics and topological descriptors provide complementary insights into the spatial organization of cells. In particular, topological features capture higher-order structural information not evident from distance-based measures alone.

Table 1: Significant spatial and topological features associated with survival outcomes in the NLST dataset.

Threshold	Feature	<i>p</i> -value
$p < 0.05$	<code>witness_tumor_stromal_h0_lifetime_max</code>	0.005
	<code>witness_tumor_stromal_h0_death_std</code>	0.018
	<code>PCF.CROSS.T2I.PC1</code>	0.028
$p < 0.10$	<code>witness_immune_stromal_h1_birth_std</code>	0.062
	<code>MK.CONN.S2I.PC2</code>	0.063
	<code>L.CROSS.T2I.PC1</code>	0.065
	<code>witness_tumor_immune_h1_death_mean</code>	0.098
$p < 0.15$	<code>J.REP.I.PC1</code>	0.104
	<code>G.CROSS.T2I.PC1</code>	0.109
	<code>K.CROSS.T2S.PC2</code>	0.143
	<code>MH.IS</code>	0.144
$p < 0.20$	<code>K.CROSS.S2I.PC1</code>	0.155
	<code>J.REP.PC2</code>	0.158
	<code>K.CROSS.T2S.PC1</code>	0.161
	<code>F.REP.I.PC2</code>	0.165
	<code>G.REP.PC2</code>	0.191

## 5.2 Case Study II: Oral Tissue Pathology Images

The OPMD dataset consisted of 255 whole-slide images acquired at 40 $\times$  magnification from 128 patients with oral premalignant lesions. Using a deep convolutional neural network developed by our team (Wang et al., 2019), nuclei were segmented and classified into four distinct categories: basal, other epithelial, lymphocytes, and stromal cells. For feature computation, only three types—basal, lymphocyte, and stromal cells—were used, excluding the other epithelial category. This resulted in 703 segmented image regions, each containing approximately 1000 cell points.

Spatial analysis of the OPMD dataset revealed distinct predictors associated with patient survival. Table 2 summarizes the significant features identified across different  $p$ -value thresholds. The complete set of results is provided in Supplementary Table 2.

At the most stringent level ( $p < 0.05$ ), J.REP.T.PC2 emerged as one of the strongest predictors, representing empty-space dynamics in tumor cell organization. Notably, topological features were also significant, including the number of loops created (`witness_tumor_stromal_h1_n_features`) and the number of connected components (`witness_tumor_immune_h0_n_features`), indicating the importance of loop and connected component counts in tumor-stromal and tumor-immune organization.

When the threshold was relaxed to  $p < 0.10$ , additional predictors became significant, including J.REP.PC2, J.CROSS.T2I.PC2, and J.REP.S.PC2, along with topological features such as `witness_tumor_stromal_h0_death_std` and `witness_tumor_stromal_h0_n_features`.

Expanding the criterion to  $p < 0.15$  revealed further cross-type spatial descriptors, including G.CROSS.T2I.PC2 and PCF.CROSS.T2I.PC2. At  $p < 0.20$ , additional features reached significance, such as G.REP.PC2, MK.CONN.T2S.PC2, and PCF.CROSS.S2I.PC2, together with several similarity indices, including Jaccard.IS and Dice.IS.

Overall, the OPMD dataset exhibited a distinct pattern of significant spatial predictors compared with the NLST cohort, with  $J$ -functions and topological feature counts playing a prominent role in survival prediction.

Table 2: Significant spatial and topological features associated with survival outcomes in the OPMD dataset.

Threshold	Feature	$p$ -value
$p < 0.05$	witness_tumor_stromal_h1_n_features	0.011
	J.REP.T.PC2	0.020
	witness_tumor_immune_h0_n_features	0.023
$p < 0.10$	J.REP.PC2	0.067
	J.CROSS.T2I.PC2	0.071
	J.REP.S.PC2	0.083
	witness_tumor_stromal_h0_death_std	0.090
	witness_tumor_stromal_h0_n_features	0.099
$p < 0.15$	G.CROSS.T2I.PC2	0.117
	PCF.CROSS.T2I.PC2	0.142
$p < 0.20$	PCF.CROSS.S2I.PC2	0.165
	Dice.IS	0.171
	Jaccard.IS	0.172
	MK.CONN.T2S.PC2	0.178
	G.REP.PC2	0.187

### 5.3 Threshold-based Significance Analysis

In the NLST dataset, 16 spatial features reached significance at  $p < 0.20$ , with 11 features remaining significant at  $p < 0.15$ , 7 features at  $p < 0.10$ , and 3 features at  $p < 0.05$ . Similarly, the OPMD dataset demonstrated 15 significant features at  $p < 0.20$ , 10 features at  $p < 0.15$ , 8 features at  $p < 0.10$ , and 3 features achieving significance at  $p < 0.05$ . This gradient of statistical significance suggests that spatial organization encodes meaningful prognostic information, although the effect sizes may be subtle due to the inherent variability in cellular spatial arrangements within tumor tissue architecture and other domain knowledges such as tumor size in different types of cancers.

The use of multiple significance thresholds is justified by several factors inherent to spatial point pattern analysis. First, the resolution and density of marked point pattern data

can influence the sensitivity of spatial statistics to detect biologically relevant structures. Second, the complex multi-scale nature of tumor spatial organization may yield moderate rather than strong statistical associations. Third, the exploratory nature of comprehensive spatial feature analysis warrants consideration of features that may achieve stronger significance in larger cohorts or independent validation datasets.

## 6 Conclusion

The spatial organization of cells within tumor tissue carries critical information about disease progression and patient outcomes, yet accessible computational tools for rigorous quantification of these spatial patterns have remained limited. We developed SASHIMI, a web-based framework that integrates diverse spatial statistics, topological features, and areal similarity indices to enable systematic extraction and analysis of spatial biomarkers from AI-segmented histopathology images.

SASHIMI addresses key limitations in existing approaches by providing a comprehensive suite of 27 spatial features derived from single-type, cross-type interactions, and topological characteristics. To our knowledge, this is the first publicly available platform that combines this breadth of spatial analytical methods with real-time computation and interactive visualization in an accessible web interface. The framework extends beyond exploratory visualization by enabling direct integration of extracted features into downstream statistical and machine learning workflows, facilitating spatial biomarker discovery for researchers without specialized computational expertise.

While designed for computational pathology applications, the framework’s foundation in marked point pattern analysis makes it applicable to any spatial context involving point pattern data with categorical labels. Future developments will focus on enhancing computational scalability through parallel processing architectures and incorporating automated

nuclei detection capabilities to enable direct analysis of raw histopathology slides. By bridging rigorous spatial statistics with accessible biomedical applications, SASHIMI provides a systematic approach to quantifying spatial inter-play between cells in tumor tissue organization and investigating how spatial architecture influences disease progression and clinical outcomes.

## 7 Funding

This work was partially supported by the National Institutes of Health grants R15 CA274241 (C.M.), R01GM141519 (G.X. and Q.L.), R01GM140012 (G.X.), R01GM115473 (G.X.), U01CA249245 (G.X.), the Cancer Prevention and Research Institute of Texas grant CPRIT RP230330 (G.X.), and the National Science Foundation grants DMS-2113674 (Q.L.) and DMS-2210912 (Q.L.)

## 8 Data Availability Statement

**Case study I.** The H&E-stained pathology images and patient clinical information analyzed in this study are available through the National Lung Screening Trial (NLST) data portal at <https://cdas.cancer.gov/learn/nlst/home/>. Access to the raw images requires submission of a data request through the Cancer Data Access System (CDAS). The AI-segmented images generated in this study are available from the corresponding author upon reasonable request.

**Case study II.** The OPMD dataset analyzed in this study is available in the Zenodo repository under restricted access at <https://doi.org/10.5281/ZENODO.10664056>. This dataset is described in (Piyarathne et al., 2024). The nuclei segmentation and classification results generated in this study using ConvPath (Wang et al., 2019) are available from the

corresponding author upon reasonable request.

## References

- Baddeley, A., Rubak, E. and Turner, R. (2016), *Spatial point patterns: methodology and applications with R*, CRC Press, Boca Raton, FL.
- Bivand, R., Altman, M., Anselin, L., Assunção, R., Berke, O., Bernat, A., Blanchet, G. et al. (2015), *spdep: spatial dependence: weighting schemes, statistics and models*. R package version 1.2-4.
- URL:** <https://CRAN.R-project.org/package=spdep>
- Cooper, L. A. D., Kong, J., Gutman, D. A., Dunn, W. D., Nalisnik, M. and Brat, D. J. (2015), ‘Novel genotype-phenotype associations in human cancers enabled by advanced molecular platforms and computational analysis of whole slide images’, *Lab. Investig.* **95**(4), 366–376.
- Corredor, G., Wang, X., Zhou, Y., Lu, C., Fu, P., Syrigos, K., Rimm, D. L., Yang, M., Romero, E., Schalper, K. A. et al. (2019), ‘Spatial architecture and arrangement of tumor-infiltrating lymphocytes for predicting likelihood of recurrence in early-stage non-small cell lung cancer’, *Clin. Cancer Res.* **25**(5), 1526–1534.
- De Silva, V. and Carlsson, G. E. (2004), Topological estimation using witness complexes., *in* ‘PBG’, pp. 157–166.
- Geary, R. C. (1954), ‘The contiguity ratio and statistical mapping’, *Incorpor. Stat.* **5**(3), 115–146.

- Gurcan, M. N., Boucheron, L. E., Can, A., Madabhushi, A., Rajpoot, N. M. and Yener, B. (2009), ‘Histopathological image analysis: a review’, *IEEE Rev. Biomed. Eng.* **2**, 147–171.
- Hanahan, D. and Weinberg, R. A. (2011), ‘Hallmarks of cancer: The next generation’, *Cell* **144**(5), 646–674.
- Kong, D., Ibrahim, J. G., Lee, E. and Zhu, H. (2018), ‘Flcrm: Functional linear cox regression model’, *Biometrics* **74**(1), 109–117.
- Li, Q., Wang, X., Liang, F. and Xiao, G. (2019b), ‘A Bayesian mark interaction model for analysis of tumor pathology images’, *Ann. Appl. Stat.* **13**(3), 1708–1729.
- Li, Q., Wang, X., Liang, F., Yi, F., Xie, Y., Gazdar, A. and Xiao, G. (2019a), ‘A Bayesian hidden Potts mixture model for analyzing lung cancer pathology images’, *Biostats.* **20**(4), 565–581.
- Li, X. (2024), ‘SpatialQPFs: an R package for deciphering cell-cell spatial relationship’, *bioRxiv* pp. 2024–06.
- Moon, C., Li, Q. and Xiao, G. (2023), ‘Using persistent homology topological features to characterize medical images: case studies on lung and brain cancers’, *Ann. Appl. Stat.* **17**(3), 2192–2211.
- Moran, P. A. P. (1950), ‘Notes on continuous stochastic phenomena’, *Biometrika* **37**(1–2), 17–23.
- Morisita, M. (1962), ‘I- $\sigma$  index: a measure of dispersion of individuals’, *Res. Popul. Ecol.* **4**(1), 1–7.
- Piyarathne, N. S., Liyanage, S. N., Rasnayaka, R. M. S. G. K., Hettiarachchi, P. V. K. S., Devindi, G. A. I., Francis, F. B. A. H., Dissanayake, D. M. D. R., Ranasinghe, R. A. N. S., Pavithya, M. B. D., Nawinne, I. B. et al. (2024), ‘A comprehensive dataset of

- annotated oral cavity images for diagnosis of oral cancer and oral potentially malignant disorders’, *Oral Oncol.* **156**, 106946.
- Ripley, B. D. (1977), ‘Modelling spatial patterns’, *J. R. Stat. Soc. Ser. B Stat. Methodol.* **39**(2), 172–212.
- Saltz, J., Gupta, R., Hou, L., Kurc, T., Singh, P., Nguyen, V., Samaras, D., Shroyer, K. R., Zhao, T., Batiste, R., Van Arnam, J. et al. (2018), ‘Spatial organization and molecular correlation of tumor-infiltrating lymphocytes using deep learning on pathology images’, *Cell Rep.* **23**(1), 181–193.e7.
- Sobhani, F., Muralidhar, S., Hamidinekoo, A., Hall, A. H., King, L. M., Marks, J. R., Maley, C., Horlings, H. M., Hwang, E. S. and Yuan, Y. (2022), ‘Spatial interplay of tissue hypoxia and T-cell regulation in ductal carcinoma in situ’, *NPJ Breast Cancer* **8**(1), 105.
- Stolz, B. J., Dhesi, J., Bull, J. A., Harrington, H. A., Byrne, H. M. and Yoon, I. H. R. (2024), ‘Relational persistent homology for multispecies data with application to the tumor microenvironment’, *Bull. Math. Biol.* **86**(11), 128.
- The GUDHI Project (2025), *GUDHI User and Reference Manual*, 3.11.0 edn, GUDHI Editorial Board.
- URL:** <https://gudhi.inria.fr/doc/3.11.0/>
- Van Den Bent, M. J. (2010), ‘Interobserver variation of the histopathological diagnosis in clinical trials on glioma: a clinician’s perspective’, *Acta Neuropathol.* **120**(3), 297–304.
- Vu, T., Wrobel, J., Bitler, B. G., Schenk, E. L., Jordan, K. R. and Ghosh, D. (2022), ‘SPF: a spatial and functional data analytic approach to cell imaging data’, *PLoS Comput. Biol.* **18**(6), e1009486.
- Wang, S., Rong, R., Zhou, Q., Yang, D. M., Zhang, X., Zhan, X., Bishop, J., Chi, Z.,



- Wilhelm, C. J., Zhang, S., Pickering, C. R., Kris, M. G., Minna, J., Xie, Y. and Xiao, G. (2023), ‘Deep learning of cell spatial organizations identifies clinically relevant insights in tissue images’, *Nat. Commun.* **14**(1), 7872.
- Wang, S., Wang, T., Yang, L., Yang, D. M., Fujimoto, J., Yi, F., Luo, X., Yang, Y., Yao, B., Lin, S. et al. (2019), ‘ConvPath: a software tool for lung adenocarcinoma digital pathological image analysis aided by a convolutional neural network’, *EBioMedicine* **50**, 103–110.
- Wang, X., Barrera, C., Bera, K., Viswanathan, V. S., Azarianpour-Esfahani, S., Koyuncu, C., Velu, P., Feldman, M. D., Yang, M., Fu, P. et al. (2022), ‘Spatial interplay patterns of cancer nuclei and tumor-infiltrating lymphocytes (TILs) predict clinical benefit for immune checkpoint inhibitors’, *Sci. Adv.* **8**(22), eabn3966.
- Zhai, W., Lim, T. K.-H., Zhang, T., Phang, S.-T., Tiang, Z., Guan, P., Ng, M.-H., Lim, J. Q., Yao, F., Li, Z., Ng, P. Y., Yan, J., Goh, B. K., Chung, A. Y.-F., Choo, S.-P., Khor, C. C., Soon, W. W.-J., Sung, K. W.-K., Foo, R. S.-Y. and Chow, P. K.-H. (2017), ‘The spatial organization of intra-tumour heterogeneity and evolutionary trajectories of metastases in hepatocellular carcinoma’, *Nat. Commun.* **8**(1), 4565.
- Zhang, C., Bedi, T., Moon, C., Xie, Y., Chen, M. and Li, Q. (2024), ‘Bayesian landmark-based shape analysis of tumor pathology images’, *J. Am. Stat. Assoc.* **119**(546), 798–810.
- Zhang, X., Gleber-Netto, F. O., Wang, S., Jin, K. W., Yang, D. M., Gillenwater, A. M., Myers, J. N., Ferrarotto, R., Pickering, C. R. and Xiao, G. (2023), ‘A deep learning onion peeling approach to measure oral epithelium layer number’, *Cancers (Basel)* **15**(15), 3891.